Chinese Journal of
POLYMER SCIENCE

RESEARCH ARTICLE

https://doi.org/10.1007/s10118-026-3610-0
Chinese J. Polym. Sci.

A Pyrazine-based Covalent Organic Framework as a Cathode Material for Aqueous Rechargeable Zinc-ion Batteries

Ke-Jun Jin and Ying-Jian Yu*

College of Physics Science and Technology, Kunming University, Kunming 650214, China

Electronic Supplementary Information

Abstract Aqueous zinc-ion batteries (AZIBs) are safe and cost-effective, making them ideal for large-scale energy storage and wearable electronics. Nevertheless, the advancement of AZIB technology faces constraints due to limited energy storage capability and degraded cyclability, primarily attributed to the absence of optimal cathode materials. In this study, two structurally similar but chemically different covalent organic framework materials (Aza-COF-1L and Aza-COF-2) were synthesized. Notably, Aza-COF-1L is easier to synthesize and features abundant pyrazine redox-active sites, a well-defined porous structure, and intrinsic stability. Consequently, Aza-COF-1L exhibited an electrochemical performance superior to that of Aza-COF-2. Aza-COF-1L achieved initial capacities of 368.58, 345.96, and 327.82 mAh·g^{-1} at 0.1, 0.5, and 1 A·g^{-1}, respectively. After 800 cycles at 1 A·g^{-1}, Aza-COF-1L maintains a specific capacity of 136.38 mAh·g^{-1}. In contrast, Aza-COF-2 exhibited an initial capacity of 117.79 mAh·g^{-1} at 0.1 A·g^{-1}, and its capacity significantly decreased during cycling. Additionally, the contribution of the C═N pyrazine redox site in Aza-COF-1L to battery capacity during charging and discharging was experimentally analyzed. These results provide valuable guidance for the development of high-performance organic cathode materials for use in AZIBs.

Keywords Zinc-ion batteries; Covalent organic frameworks; Cathodes; Pyrazine-based materials; Organic electrodes

Citation: Jin, K. J.; Yu, Y. J. A pyrazine-based covalent organic framework as a cathode material for aqueous rechargeable zinc-ion batteries. *Chinese J. Polym. Sci.* https://doi.org/10.1007/s10118-026-3610-0

INTRODUCTION

The depletion of global fossil fuel reserves and ongoing climate crisis have accelerated the transition to sustainable energy resources such as solar and tidal energy.[1–5] However, the intermittent nature of clean energy sources makes large-scale energy storage technology a key component of energy transition.[6–9] Although lithium-ion batteries (LIBs) have maintained market leadership owing to their superior energy density, they pose several challenges. Safety concerns regarding flammable organic electrolytes, geopolitical risks associated with lithium and cobalt resources, and challenges in battery recycling are driving the search for safer and more sustainable energy alternatives.[10–15] Compared to traditional LIBs, aqueous zinc-ion batteries (AZIBs) contain a non-flammable aqueous electrolyte, which mitigates the risk of thermal runaway. The Zn metal anode demonstrates a substantial theoretical capacity of 820 mAh·g^{-1}, and Zn is over 100 times more abundant in the Earth's crust than lithium.[16–20] Aqueous electrolytes have superior ionic conductivity, which enables batteries to achieve ultrafast charging and discharging. The cost-efficiency metrics and engineering scalability of AZIB systems demonstrate their techno-economic viability for deployment in grid-scale energy storage infrastructures and next-generation wearable electronic systems that require high energy density and mechanical flexibility. However, the development of AZIBs is primarily limited by the cathode-side issues. For many promising cathode materials (*e.g.*, layered vanadium oxides or manganese-based oxides), repeated Zn^{2+} intercalation/deintercalation can induce irreversible structural collapse or phase transitions. This degradation, coupled with active material dissolution and slow ion diffusion kinetics, severely impedes cycling stability and rate capability.[21–24] Consequently, researchers have focused on developing high-performance AZIBs using inorganic compounds as cathodes, including vanadium-based compounds, manganese-based compounds, and Prussian blue analogs.[25–28] Despite the advantages of these inorganic electrodes, the development of AZIBs is limited by their low conductivity, toxicity, and energy density.

Organic cathode materials provide a promising solution to these challenges.[29–32] Conjugated carbonyl compounds store zinc ions *via* a reversible enolate reaction, and their flexible molecular structures can accommodate volume changes. Three-dimensional networks formed by conductive polymers, such as polyaniline, provide multidimensional ion transport channels. Notably, organic materials can precisely control the redox potential through molecular engineering, which is difficult to achieve using inorganic materials.[33–36] However, organic electrodes have certain limitations that hinder their development. For example, a lack of intrinsic conductivity re-

* Corresponding author, E-mail: yuyingjiankmu@163.com
Received December 28, 2025; Accepted February 2, 2026; Published online April 24, 2026

sults in a low performance. During charging and discharging, the π-π stacking structure in organic electrodes is prone to disruption, leading to active site failure. Additionally, the low density of organic molecules results in low bulk energy density for organic electrodes.[37–40] Therefore, when designing new organic polymer cathode materials, both cycling stability and high capacity must be prioritized.

Covalent organic frameworks (COFs) represent a new class of crystalline, porous polymer-based materials owing to their well-defined porosity, predictable organization of redox-active groups, and high chemical stability.[41–43] These properties make COFs ideal candidates as cathode materials in aqueous ZIBs. Unlike amorphous organic polymers, COFs form a periodically ordered framework through strong covalent bonds, which enable precise molecular arrangement, tunable pore structures, and a stable redox environment.[44,45] The design of COFs at the molecular level is crucial for optimizing their performance. Through a modular synthesis strategy, redox-active groups can be incorporated into framework nodes or linker units to create periodically arranged active sites.[46,47] The COFs feature multidimensional channels that form homogeneous pores. These pores facilitate the rapid movement of Zn ions in the COF electrode, enabling them to reach active sites.[48,49] The highly crystalline π-conjugated framework of COFs enhances the electrode stability. The rigid covalent organic framework ensures the stability of the chemical reaction and effectively inhibits the structural degradation of the cathode.

In this study, 2D COFs (Aza-COF-1L and Aza-COF-2) were synthesized to enhance their electrochemical performance as AZIB cathodes. Aza-COF-1L was synthesized *via* a photo-induced imine condensation reaction. In this process, the photon energy accelerates the imine condensation reaction and facilitates the conversion of amorphous imines into crystalline COFs. Compared to Aza-COF-2, Aza-COF-1L has a shorter synthesis time and utilizes a more cost-effective ligand. Aza-COF-1L features dense pyrazine redox-active sites, inherent chemical stability, and a well-defined porous structure, enabling reversible and efficient zinc-ion storage during charging and discharging. Additionally, Aza-COF-1L demonstrates a superior initial capacity of 368.58 mAh·g^{-1} at 0.1 A·g^{-1} and maintains a specific capacity of 136.38 mAh·g^{-1} after 800 cycles at 1 A·g^{-1}. In contrast, Aza-COF-2 achieved an initial capacity of only 117.79 mAh·g^{-1} at 0.1 A·g^{-1}, and its specific capacity significantly decreased within the first 100 cycles. The Aza-COF-1L-based electrode exhibited excellent initial capacity and cycling stability, making it a viable option for AZIB cathode applications.

EXPERIMENTAL

Materials

The following chemicals were used: hexaketocyclohexane octahydrate (HCH, ≥99%), 1,2,4,5-benzenetetramine tetrahydrochloride (BTA·4HCl, ≥97%), methanol (≥99.8%), mesitylene, acetic acid (≥99%) 2,3,6,7,10,11-hexaaminotriphenylene hexahydrochloride (HATP·6HCl, ≥95%), 1,3-dimethyl-2-imidazolidinone (DMI), sulfuric acid (H_2SO_4), acetone, 1-methyl-2-pyrrolidinone (NMP ≥99.9%), conductive carbon black (Super P), polyvinylidene difluoride (PVDF), zinc sulfate ($ZnSO_4$), and manganese sulfate ($MnSO_4$).

Synthesis Methods

Synthesis of Aza-COF-1L:[50] BTA·4HCl (213 mg, 0.75 mmol) and HCH (156 mg, 0.5 mmol) were added to quartz bottles. The precursors were dissolved by adding 60 mL of a solvent mixture of methanol/mesitylene at a 1:1 volume ratio under argon protection. After 30 min of sonication, 12 mL of distilled water and 18 mL of acetic acid were injected into quartz bottles to induce the reaction. The reaction was carried out under xenon irradiation. The resulting powder precipitate was washed thrice with methanol and mesitylene.

Synthesis of Aza-COF-2:[51] HATP·6HCl (289 mg, 0.5 mmol) and HCH (156 mg, 0.5 mmol) were dissolved in 50 mL of DMI, and 10 drops of sulfuric acid (98%) were slowly added to the mixture. The reaction flask was heated to 60 °C for 4 h under a N_2 atmosphere. Subsequently, the temperature was increased to 175 °C and maintained for five days. The flask was cooled to room temperature and the solid product was collected. The resulting powder precipitate was washed thrice with distilled water and acetone.

Physical and Spectroscopic Characterization

The functional groups of the COF materials were characterized using Fourier-transform infrared spectroscopy (FTIR, Nexus 670). The thermogravimetric analysis (TGA) curve has been tested under the following conditions: using a Netzsch STA 449F3 thermal analyzer, heating from 30 °C to 1000 °C at a rate of 10 °C·min^{-1} in a nitrogen atmosphere (250.0 mL·min^{-1}). The specific surface area and pore distribution of the COF powders were determined using a fully automated Brunauer-Emmett-Teller (BET) surface and porosity analyzer (Micromeritics 3Flex). The structural properties of the COF materials were investigated by powder X-ray diffraction (PXRD, Ultima IV). The morphology of the COF powders and the elemental distribution of the COF cathodes were examined using scanning electron microscopy (SEM, Sigma 300). The crystal structures of the COF powders were evaluated using transmission electron microscopy (TEM, FEI Tecnai F20). The elemental composition of the COF cathode was analyzed semi-quantitatively using X-ray photoelectron spectroscopy (XPS, Thermo Kalpha).

Coin-Cell Assembly

An active compound (Aza-COF-1L/Aza-COF-2), a conductive material (Super P), and a binder (PVDF) were mixed in a mass ratio of 6:3:1 to prepare the cathode material. These components were combined with NMP as a solvent to form a slurry, which was then coated onto a stainless-steel mesh using a scraper. The film was dried in a vacuum oven at 65 °C for 6 h. The cathode was assembled into a CR2032 coin battery, with a zinc metal sheet as the anode. The battery contained a separator and an electrolyte solution composed of $ZnSO_4$/$MnSO_4$ at a molar ratio of 2:0.1.

Electrochemical Measurements

Electrochemical testing of all coin cells was conducted at ambient temperature. The long-term cycling stability, constant current charge/discharge performance, and rate capability of the batteries were analyzed using a coin-cell analyzer (Neware CT-4008T-5V10mA). Cyclic voltammetry (CV) measurements were performed using a potentiostat (CHI660E).

https://doi.org/10.1007/s10118-026-3610-0

RESULTS AND DISCUSSION

Synthesis and Characterization

Aza-COF-1L was synthesized *via* a photoinduced imine condensation reaction between BTA·4HCl and HCH. Aza-COF-2 was synthesized *via* an acid-catalyzed solvothermal reaction between HATP·6HCl and HCH (Fig. 1a). The successful formation of Aza-COF-1L and Aza-COF-2 was confirmed by FTIR spectroscopy. The FTIR spectrum of Aza-COF-1L (Fig. 1b) exhibits two strong bands at 1593 and 1244 cm^{-1}, corresponding to the

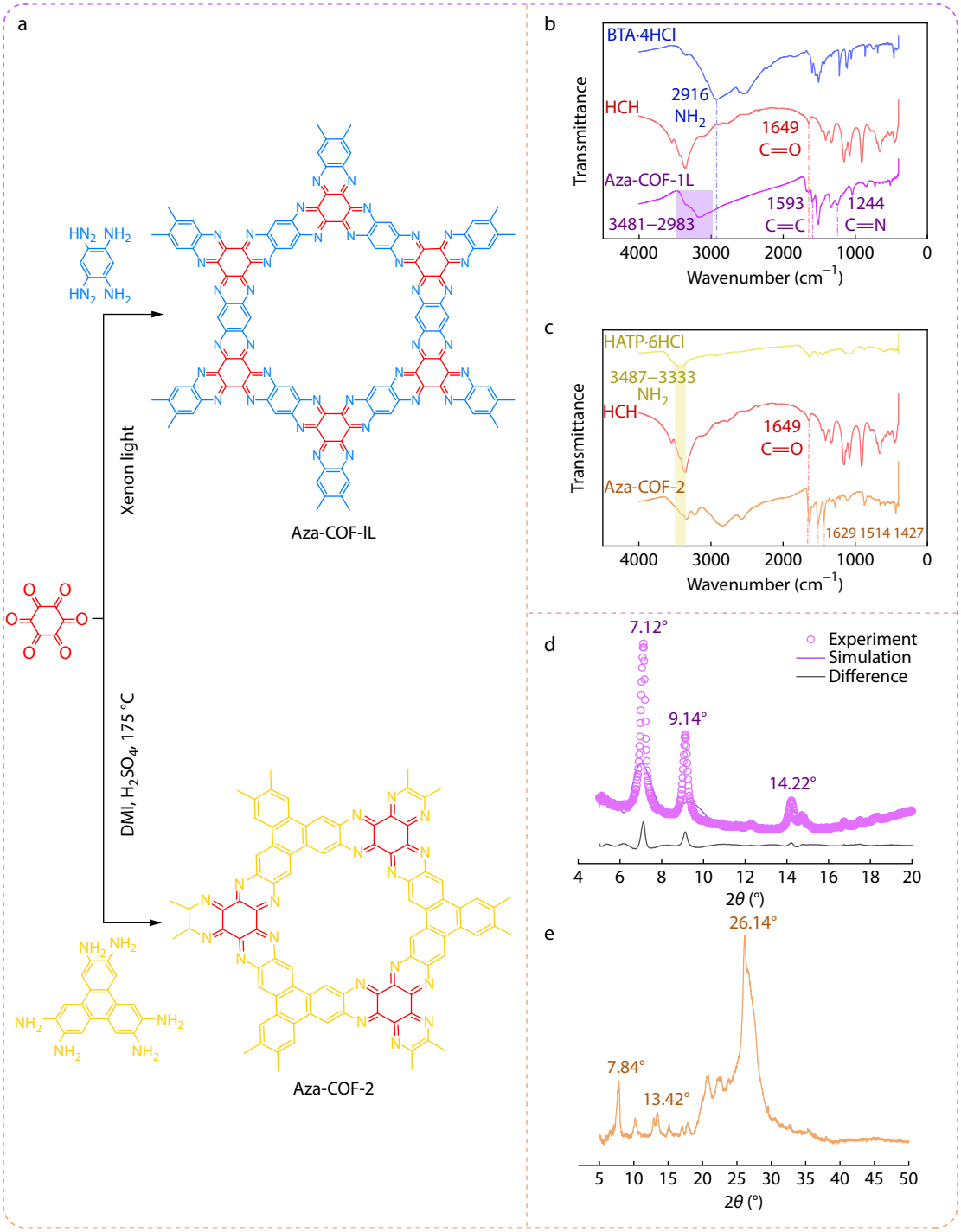

Fig. 1 (a) Schematic of the synthesis process for Aza-COF-1L and Aza-COF-2; (b) FTIR spectra comparison of BTA·4HCl (blue), HCH (red), Aza-COF-1L (purple); (c) FTIR spectra comparison of HATP·6HCl (yellow), HCH (red), and Aza-COF-2 (orange); (d) Experimental and simulated PXRD patterns of Aza-COF-1L (the dark purple line plot represents the experimental pattern, the light purple scatter plot represents the simulated pattern, and the gray line plot corresponds to the difference profile between them); (e) Experimental PXRD pattern of Aza-COF-2.

https://doi.org/10.1007/s10118-026-3610-0

C=C and C=N stretching vibrations of the pyrazine functional groups. The absence of the characteristic NH_2 band at 2961 cm^{-1} in BTA·4HCl and the C=O stretching band at 1649 cm^{-1} in HCH confirmed the complete consumption of reactants. The broad vibrational band observed between 2983 and 3481 cm^{-1} can be attributed to water molecules adsorbed in the Aza-COF-1L pores. The FTIR spectrum of Aza-COF-2 (Fig. 1c) displays strong bands at 1629, 1514, and 1427 cm^{-1}, which are characteristic of phenazine functional groups. The absence of the NH_2 band (3487–3333 cm^{-1}) in HATP·6HCl and C=O band (1649 cm^{-1}) in HCH confirmed the complete consumption of the reactants. The results showed that at 200 °C, the mass loss of Aza-COF-1L was 23.9%, while that of Aza-COF-2 was 4.62%. The maximum rate of mass change for the former is –3.94%·min^{-1} at 117.9 °C, and for the latter, it is –2.81%·min^{-1} at 290.0 °C (Fig. S1 in the electronic supplementary information, ESI). Overall, Aza-COF-2 exhibited better thermal stability. Moreover, the permanent porosities of both COFs were assessed through N_2 adsorption-desorption measurements at −196 °C (Fig. S2 in ESI). The isotherms of Aza-COF-1L and Aza-COF-2 at −196 °C (Fig. S3 in ESI) show a Type II-like profile with pronounced uptake at high relative pressures and a small hysteresis loop, which suggests limited accessible microporosity. Aza-COF-1L and Aza-COF-2 exhibited surface areas of 25.77 and 66.11 $m^2 \cdot g^{-1}$, respectively.

The crystal structure characteristics of Aza-COF-1L and Aza-COF-2 were analyzed using PXRD. The PXRD pattern of Aza-COF-1L (Fig. 1d) revealed strong peaks at 2θ=7.12° and 2θ=9.14° and weaker peaks at 2θ=14.22°. These peaks correspond to the (200), (210), and (301) crystal planes. Aza-COF-1L had a hexagonal pore size of about 12.4 Å. Specifically, a periodic structural model of Aza-COF-1L was constructed and geometrically optimized using the Forcite module in Materials Studio (Fig. S4 in ESI). Based on this optimized model, a simulated PXRD pattern was generated and compared with the experimental PXRD pattern. The revised figure shows that the simulated pattern reproduces the key diffraction features of Aza-COF-1L, supporting updated structural assignment and peak indexing. We simulated the AA and AB stacks of Aza-COF-1L, and we further performed Pawley refinement against the experimental PXRD pattern, and obtained the fitting statistics, and found that the synthesized Aza-COF-1L material was more in line with the AB stack (weighted R-factor (Rwp) = 11.84%, R-factor (Rp) = 6.75%). The PXRD pattern of Aza-COF-2 (Fig. 1e) showed strong peaks at 2θ=7.84°, 13.42°, and 26.14°, corresponding to the (100), (110), and (001) diffraction planes, respectively. Aza-COF-2 has a hexagonal pore size of about 11.26 Å. The peak at 2θ=26.14° corresponded to an interlayer distance of 3.40 Å.

The morphologies of Aza-COF-1L (Fig. 2a) and Aza-COF-2 (Fig. 2b) were examined by SEM. The Aza-COF-1L powder exhibited a uniformly shaped rod-like structure with diameters of about 100–200 nm. However, the surface of the Aza-COF-2 powder consisted of small finely ground particles. Both COFs exhibited a two-dimensional (2D) layered stacked morphology. TEM images of Aza-COF-1L (Fig. 2c) and Aza-COF-2 (Fig. 2d) revealed a layered sheet arrangement. Additionally, the TEM image of Aza-COF-1L shows distinct lattice fringes (Fig. 2e), confirming the good crystallinity of Aza-COF-1L.

Electrochemical Characterization

The ordered porous structure and high-density pyrazine redox-active sites in Aza-COF-1L are particularly beneficial for Zn^{2+} storage in electrodes. These properties provide ion diffusion channels and enhance Zn^{2+} storage efficiency. To evaluate the performance of Aza-COF-1L as a potential AZIB cathode material, electrochemical tests were conducted using a typical coin cell (Fig. 3a). The cell was assembled with a Zn foil anode, glass fiber separator, and electrolyte incorporating 2 mol·L^{-1} $ZnSO_4$ and 0.1 mol·L^{-1} $MnSO_4$. Fig. 3(b) shows the CV curves of Aza-COF-1L and

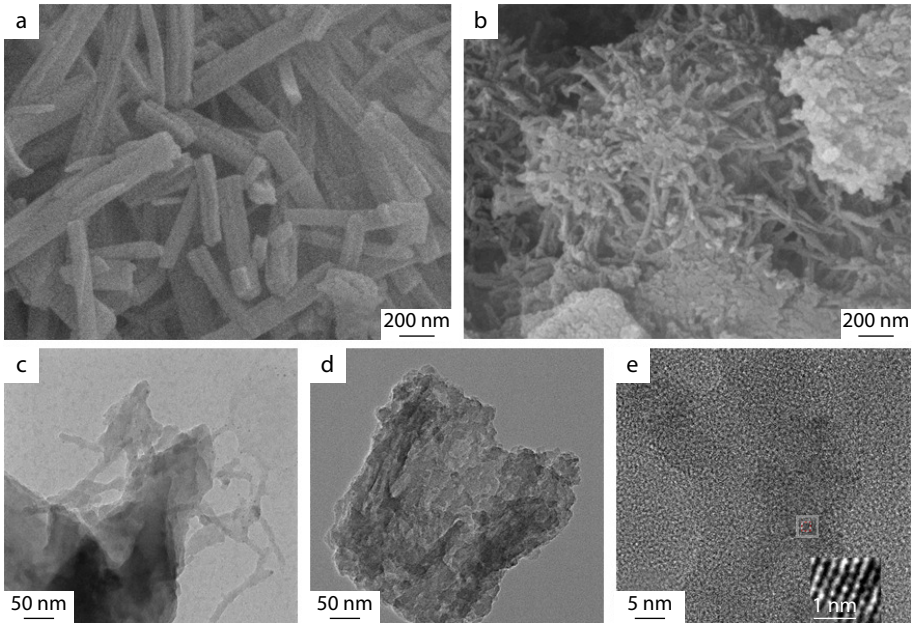

Fig. 2 (a) SEM image of Aza-COF-1L (scale bar: 200 nm); (b) SEM image of Aza-COF-2 (scale bar: 200 nm); (c) TEM image of Aza-COF-1L (scale bar: 50 nm); (d) TEM image of Aza-COF-2 (scale bar: 50 nm); (e) TEM image of Aza-COF-1L (scale bar: 5 nm, the scale bar of the inset is 1 nm).

https://doi.org/10.1007/s10118-026-3610-0

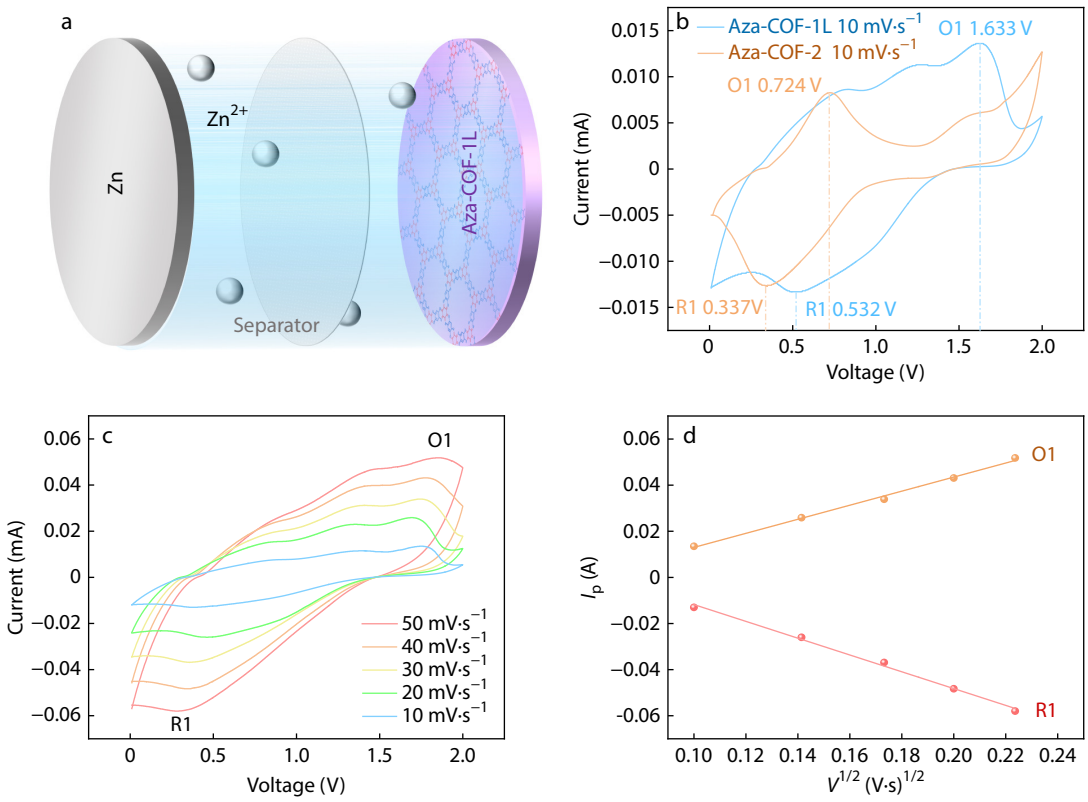

Fig. 3 (a) Schematic of the aqueous Zn/Aza-COF-1L battery; (b) CV curves of Aza-COF-1L and Aza-COF-2 at a scan rate of 10 mV·s^{-1}; (c) CV curves of the Zn/Aza-COF-1L battery at scan rates of 10, 20, 30, 40, and 50 mV·s^{-1}, respectively; (d) Linear fitting of the peak current (I_p) versus the square root of the scan rate ($V^{1/2}$) for the Zn/Aza-COF-1L battery at the corresponding scan rates.

Aza-COF-2 within a voltage window of 0.01–2 V (versus Zn^{2+}/Zn) at a scanning rate of 10 mV·s^{-1}. The CV curve of Aza-COF-1L revealed a pair of redox peaks at 1.633 and 0.532 V. The CV curve of Aza-COF-2 displayed redox peaks at 0.724 and 0.337 V. The enclosed area under the CV curve of Aza-COF-1L is larger than that of Aza-COF-2. The area under the CV curve corresponds directly to the charge storage capacity of the electrode material. A larger area indicates a more significant redox reaction within a specific voltage window, indicating that the electrode material can store or release more charge. This suggests that the Zn/Aza-COF-1L battery had a higher charge storage capacity. The CV curves of Aza-COF-1L, recorded at different scan rates (Fig. 3c), revealed a linear relationship between the peak current (I_P) and the square root of the scan rate ($v^{\frac{1}{2}}$) (Fig. 3d). This indicated that the kinetics of the redox reactions were governed by the Zn^{2+} diffusion process. The Aza-COF-1L cathode had a Zn ion diffusion coefficient of about 6.423×10^{-8} cm^2·s^{-1}, as calculated from the Randles-Sevcik equation (in ESI).

The cycling stabilities of Zn/Aza-COF-1L and Zn/Aza-COF-2 were evaluated at 0.1, 0.5, and 1 A·g^{-1} (Figs. 4a–4c). Under the same cycling conditions, Zn/Aza-COF-1L consistently exhibited significantly higher specific capacities than those of Aza-COF-2. Notably, Zn/Aza-COF-1L exhibited excellent long-term cycling stability at 1 A·g^{-1} and retained a capacity of 136.38 mA·h·g^{-1} after 800 cycles. After 200 cycles, the capacity retention remains at 64.6% (Fig. S5 in ESI). The long-term cycling stability of the Aza-COF-1L cathode was further confirmed by its near-100% Coulombic efficiency throughout the cycling process. The energy storage behaviors of Zn/Aza-COF-1L and Zn/Aza-COF-2 are illustrated by their galvanostatic charge-discharge (GCD) curves at varying current densities (Fig. 4d). Zn/Aza-COF-1L exhibits a high initial specific capacity of 368.58 mAh·g^{-1} at 0.1 A·g^{-1}, with corresponding capacities of 345.96 and 327.82 mAh·g^{-1} at 0.5 and 1.0 A·g^{-1}, respectively. In contrast, Zn/Aza-COF-2 achieves lower initial specific capacities of 117.79, 98.02, and 75.39 mAh·g^{-1} at 0.1, 0.5, and 1.0 A·g^{-1}, respectively, which are significantly lower than those of Aza-COF-1L. To evaluate the fast charge-exchange kinetics during Zn insertion and extraction, we tested the rate capability of the cell (Fig. 4e). During the test, the current density was increased from 0.1 A·g^{-1} to 2.0 A·g^{-1} and then decreased back to 0.1 A·g^{-1}. Zn/Aza-COF-1L exhibits reversibility, with its specific capacity restoring from 263.28 mAh·g^{-1} to 254.64 mAh·g^{-1}, resulting in a capacity recovery rate of 96.72%. Conversely, the specific capacity of Zn/Aza-COF-2 recovers from 76.22 mAh·g^{-1} to 72.61 mAh·g^{-1}, with a 95.26% capacity recovery. This indicates that Aza-COF-1L exhibits faster charge exchange kinetics during zinc ion insertion and extraction. The improved performance of Aza-COF-1L can be attributed to its larger pore size, which shortens the ion diffusion path, enhances ion migration, and optimizes rate capability and capacity. To further clarify the inferior electrochemical performance of Aza-COF-2, the influence of the structural and chemical differences between Aza-COF-2 and Aza-COF-1L was systematically analyzed. Although both materials share an aza-linked framework, their π-conjugated building

https://doi.org/10.1007/s10118-026-3610-0

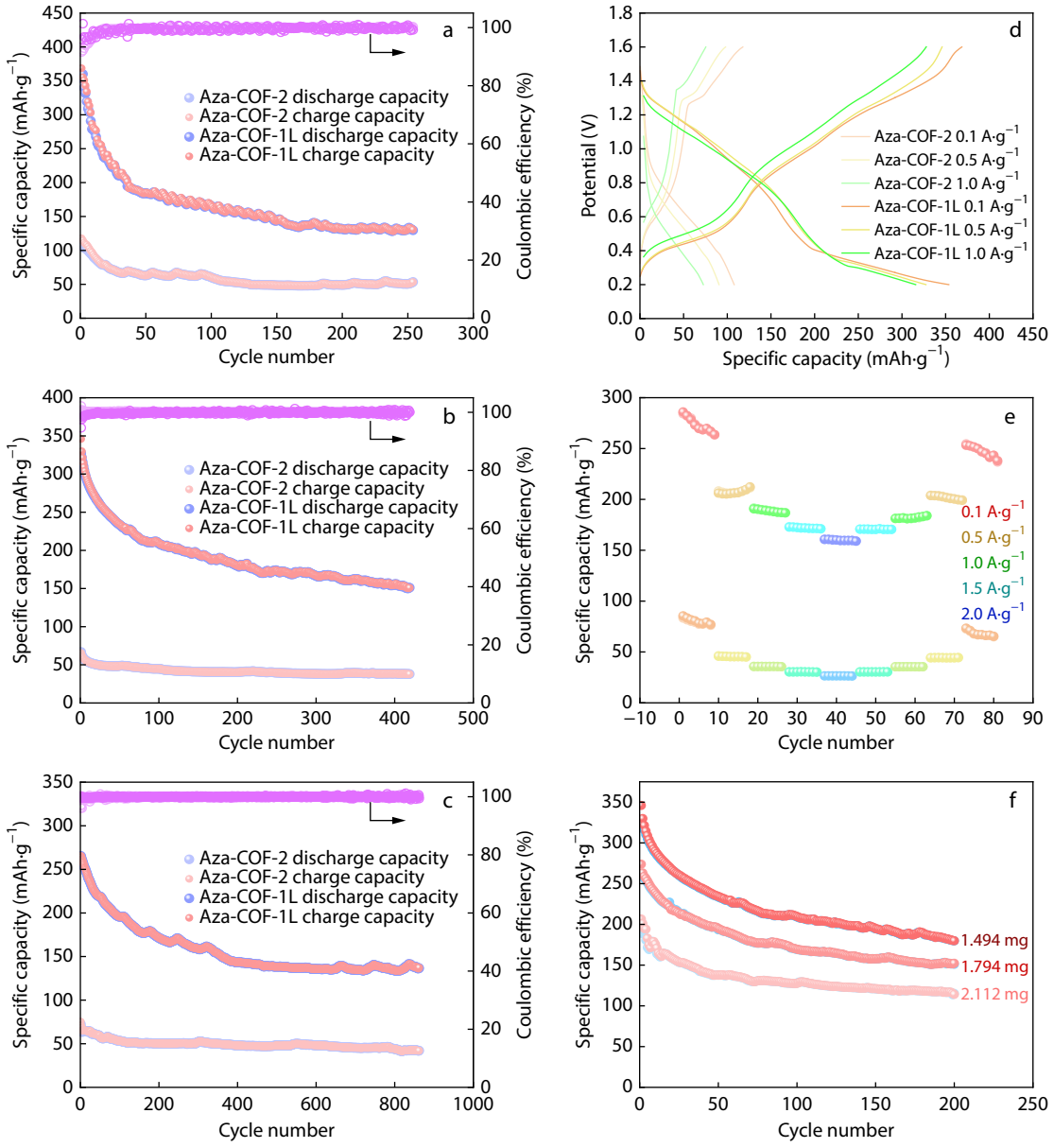

Fig. 4 Cycle stability of Zn/Aza-COF-1L and Zn/Aza-COF-2 batteries at (a) 0.1 $A \cdot g^{-1}$, (b) 0.5 $A \cdot g^{-1}$, and (c) 1.0 $A \cdot g^{-1}$; (d) GCD curves of Zn/Aza-COF-1L and Zn/Aza-COF-2 batteries at 0.1, 0.5, and 1.0 $A \cdot g^{-1}$; (e) Rate capability of Zn/Aza-COF-1L (dark color) and Zn/Aza-COF-2 (light color) batteries at various current densities of 0.1, 0.5, 1.0, 1.5, and 2.0 $A \cdot g^{-1}$; (f) Effect of active material loading on the capacity of Zn/Aza-COF-1L batteries at 0.5 $A \cdot g^{-1}$.

units and framework topologies are distinctly different. Aza-COF-1L was constructed from pyrazine-based units, resulting in a higher density of electrochemically active C=N sites per unit mass, whereas the phenazine-based building blocks in Aza-COF-2 reduced the effective redox site density, thereby limiting its Zn^{2+} storage capacity. In addition, the more rigid π-conjugated framework of Aza-COF-2 was less adaptable to repeated Zn^{2+} insertion/extraction during cycling, which likely contributed to its faster capacity decay. In contrast, the relatively flexible framework of Aza-COF-1L enabled more reversible redox reactions and improved cycling stability. Collectively, these structural and kinetic factors explain the inferior electrochemical performance of Aza-COF-2. During the recovery process, no significant difference in performance was observed between the two batteries before and after the capacity recovery. This indicates that the redox reactions in both systems are reversible. Additionally, we investigated the effect of active material loading on the cell capacity at 0.5 $A \cdot g^{-1}$ (Fig. 4f). The batteries exhibit specific capacities of 179.77, 150.99, and 115.24 $mAh \cdot g^{-1}$, corresponding to active material masses of 1.494, 1.794, and 2.112 mg, respectively. A lower active loading results in a higher specific capacity for the battery. SEM analysis was performed to examine the structural stability and morphological changes in the Aza-COF-1L cathode during charging and discharging. No by-products or significant morphological changes were observed in the electrode (Fig. S6 in ESI), thus confirming the stability of Aza-COF-1L. These results indicate that the

https://doi.org/10.1007/s10118-026-3610-0

Zn/Aza-COF-1L battery exhibits favorable energy storage performance, satisfying the criteria of high capacity and stable cycling.

Analysis of Charge-discharge Processes

To gain deeper insight into the charge–discharge mechanism of Aza-COF-1L, *ex situ* X-ray photoelectron spectroscopy (XPS) was employed to investigate the reversibility of Zn^{2+} insertion/extraction at the cathode. The C 1s peak (284.8 eV), corresponding to the C—C/C=C species, was used as an internal reference. As shown in Figs. 5(a)–5(c), the pristine electrode exhibited a distinct C=N peak centered at 287.2 eV, which originated from the imine moieties in the Aza-COF-1L framework. Upon discharge, the intensity of the C=N peak markedly decreased and a new peak appears at 286.7 eV, which can be assigned to the reduced C—N species. This evolution indicated the participation of imine units in the redox reaction, accompanied by Zn^{2+} insertion. Notably, upon subsequent charging, the C=N peak was largely restored, whereas the C—N component diminished, demonstrating a highly reversible C=N ↔ C —N conversion during repeated Zn^{2+} insertion/extraction. In contrast, the C=C and C—C components showed negligible changes throughout the charge-discharge process, suggesting that the carbon backbone remained electrochemically inert and structurally stable. These results confirm that the reversible redox reaction at the nitrogen-containing imine sites is the dominant contributor to the capacity of Aza-COF-1L, rather than irreversible structural degradation or side reactions. Further evidence of the Zn^{2+} storage mechanism in Aza-COF-1L was obtained from *ex situ* Fourier-transform infrared (FTIR) spectroscopy (Fig. S7 in ESI). Compared with the pristine electrode, the FTIR spectrum of the elec-

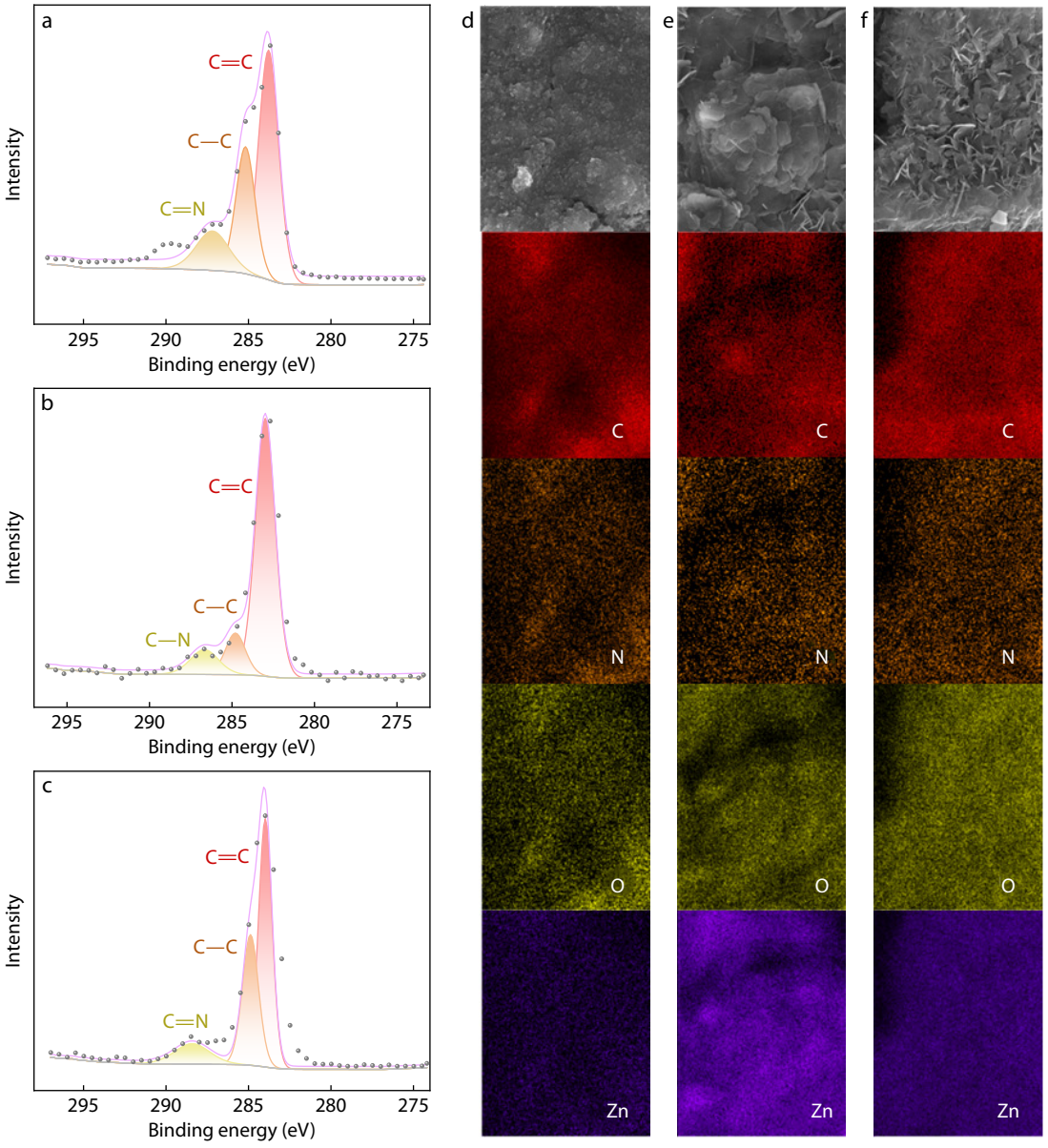

Fig. 5 Deconvoluted C 1s XPS spectra of (a) Aza-COF-1L, (b) discharged Aza-COF-1L, and (c) charged Aza-COF-1L electrodes. SEM mapping images of C, O, N, and Zn elemental distributions on the Aza-COF-1L electrode in (d) pristine, (e) discharged, and (f) charged states.

https://doi.org/10.1007/s10118-026-3610-0

trode discharged to 0.2 V exhibits newly emerged absorption bands in the range of about 955–1213 cm^{-1}, which are attributed to the coordination interaction between Zn^{2+} ions and the nitrogen atoms in the pyrazine units. These coordination-induced vibrational features disappear upon subsequent charging, indicating the effective decoordination and extraction of Zn^{2+} ions from the Aza-COF-1L framework.[52] The reversible appearance and disappearance of these bands further corroborated the dynamic and reversible Zn^{2+}–N coordination process during cycling. Such reversible coordination behavior plays a crucial role in stabilizing redox-active imine sites and enhancing Zn^{2+} utilization, thereby contributing to the high reversible capacity observed for Aza-COF-1L. Notably, the C=C expansion band (1554–1659 cm^{-1}) remains unchanged throughout the battery cycle. This confirms that the C=C bond does not contribute to the observed total specific capacity as an active site, and highlights the structural stability of the Aza-COF-1L cathode. *Ex situ* C 1s XPS (Figs. 5a–5c) and FTIR spectroscopy (Fig. S7 in ESI) revealed a highly reversible C=N ↔ C−N coordination/redox process associated with Zn^{2+} insertion/extraction, while SEM images after cycling (Figs. 5d–5f and Fig. S6 in ESI) showed no obvious byproduct formation or morphological degradation. These results collectively demonstrated the structural stability and reversibility of Aza-COF-1L during cycling.

CONCLUSIONS

In this study, we investigated the potential of crystalline porous Aza-COF-1L as a ZIB cathode. Aza-COF-1L was synthesized by a simple, fast, and efficient light-assisted method. The dense pyrazine-based redox-active sites in Aza-COF-1L, combined with its uniform porous structure and structural stability, facilitate the storage and diffusion of Zn ions. The AZIBs assembled with the Aza-COF-1L electrode exhibited excellent initial specific capacities at different current densities. Within the current density range of 0.1–2 $A{\cdot}g^{-1}$, the battery achieved excellent rate capability. The Zn/Aza-COF-1L battery exhibited an initial capacity of 368.58 $mAh{\cdot}g^{-1}$ at 0.1 $A{\cdot}g^{-1}$. After 800 cycles at 1 $A{\cdot}g^{-1}$, the battery retained a specific capacity of 136.38 $mAh{\cdot}g^{-1}$. In contrast, the Zn/Aza-COF-2 battery featured an initial capacity of 117.79 $mAh{\cdot}g^{-1}$ at 0.1 $A{\cdot}g^{-1}$, and its capacity rapidly decreased during cycling. In addition, the mechanism of zinc ion insertion into the C=N bond in the pyrazine active site of the Aza-COF-1L cathode was investigated experimentally. It should be noted that, while this work systematically investigated the cycling stability, rate capability, and Zn^{2+} storage mechanism of Aza-COF-based aqueous ZIBs, other practical performance metrics, such as calendar life and self-discharge behavior, were not evaluated in the present study. These factors are strongly influenced by long-term interfacial stability, electrolyte-electrode interactions, and parasitic side reactions in aqueous systems. A comprehensive assessment of the calendar life and self-discharge characteristics will be the subject of future investigations aimed at further advancing the practical applicability of Aza-COF-based cathode materials. The excellent performance of the Zn/Aza-COF-1L battery highlights its potential for designing high-performance, sustainable COF cathodes for AZIBs.

Conflict of Interests

The authors declare no interest conflict.

Electronic Supplementary Information

Electronic supplementary information (ESI) is available free of charge in the online version of this article at http://doi.org/10.1007/s10118-026-3610-0.

Data Availability Statement

Data will be available on request from the corresponding author upon reasonable request.

ACKNOWLEDGMENTS

This work was financially supported by the National Natural Science Foundation of China (No. 62464010), Spring City Plan-Special Program for Young Talents (No. K202005007), Yunnan Talents Support Plan for Young Talents (No. XDYC-QNRC-2022-0482), Xing Dingyu Academician Workstation of Yunnan Province (No. 202605 AF350035), and the Frontier Research Team of Kunming University 2023.

REFERENCES

1 Aridi, R.; Aridi, M.; Pannier, M. L.; Lemenand, T. Eco-environmental, and social impacts of producing electricity with various renewable energy sources. *Energy* **2025**, *20*, 135139.
2 Zhang, Y. H.; Han, Y.; Deng, F. J.; Zhao, T. Y.; Liu, Z.; Wang, D. X.; Luo, J. L.; Yu, Y. J. Enhancement of the performance of Ge-air batteries under high temperatures using conductive MOF-modified Ge anodes. *Carbon Energy* **2024**, *6*, e580.
3 Ashrafuzzaman, M.; Kalam, A.; Al-Sehemi, A. G.; Yadav, P.; Dubey, M. A review of photoanode materials, challenges, and outlook of dye-sensitized solar cells. *J. Power Sources* **2025**, *638*, 236636.
4 Zhang, P. F.; Wei, M. H.; Wang, K. L.; Wang, H. W.; Zuo, Y. Y.; Zhang, M. X. Performance optimization of zinc-air batteries *via* nanomaterials. *Energy Storage Mater.* **2025**, *75*, 104109.
5 Dash, M.; Dubey, A. K.; Choudhary, T.; Liu, Y.; Nanda, H. S.; Pati, S. Critical metal extraction from spent battery cathodes and anticipated developments using next generation green solvents for achieving a net-zero future. *Chem. Eng. J.* **2025**, *507*, 160324.
6 Jin, K. J.; Yu, Y. J. Principles, progress, and prospects of photo-rechargeable zinc-ion batteries. *J. Energy Chem.* **2025**, *104*, 382−396.
7 Zhao, Y. J.; Zheng, M. L. Battery management system for zinc-based flow batteries: a review. *Renew. Sust. Energy Rev.* **2025**, *215*, 115604.
8 Guo, X. J.; Yang, Y.; Shi, C. W.; Xu, M. J.; Liu, Y. F.; Zou, D. Q. Monitoring and control of internal temperature in power batteries: a comprehensive review. *Energy Storage Mater.* **2025**, *75*, 104051.
9 Chen, J. C.; Luo, J. L.; Xiang, Y. L.; Yu, Y. J. Light-assisted rechargeable zinc-air battery: mechanism, progress, and prospects. *J. Energy Chem.* **2024**, *91*, 178−193.
10 Li, R. S.; Zhao, W. Y.; Li, R. M.; Gan, C. L.; Chen, L.; Wang, Z. T.; Yang, X. W. Leveraging machine learning for accelerated materials innovation in lithium-ion battery: a review. *J. Energy Chem.* **2025**, *106*, 44−62.

Graphical Abstract

A Pyrazine-based Covalent Organic Framework as a Cathode Material for Aqueous Rechargeable Zinc-ion Batteries

Ke-Jun Jin, and Ying-Jian Yu

Kunming University

Aza-COF-1L with dense pyrazine redox sites was synthesized *via* a fast light-assisted method. It exhibits high capacity and stability as a superior cathode for zinc-ion batteries.

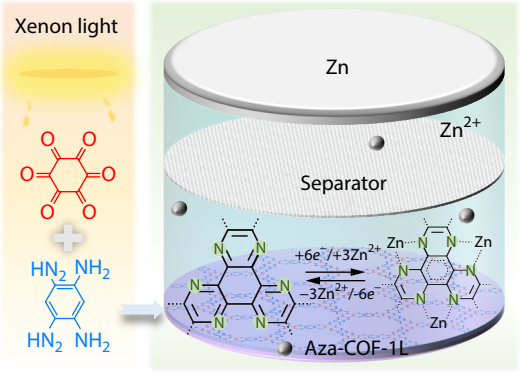

Chinese J. Polym. Sci., 2026 *https://doi.org/10.1007/s10118-026-3610-0*

11 Shi, H. Y.; Zhang, J. F.; Ou, L. M. A comprehensive review: evaluating emerging green leaching technologies for recycling spent lithium-ion batteries. *Chem. Eng. J.* **2025**, *506*, 160006.
12 Wang, Z. Y.; Du, Z. J.; Wang, L. Q.; He, G. J.; Parkin, I. P.; Zhang, Y. F.; Yue, Y. Z. Disordered materials for high-performance lithium-ion batteries: a review. *Nano Energy* **2024**, *121*, 109250.
13 Yang, M. X.; Sun, X. F.; Liu, R.; Wang, L. Z.; Zhao, F.; Mei, X. S. Predict the lifetime of lithium-ion batteries using early cycles: a review. *Appl. Energy* **2024**, *376*, 124171.
14 Hu, X. K.; Wang, Y.; Feng, X. N.; Wang, L.; Ouyang, M. G.; Zhang, Q. Thermal stability of ionic liquids for lithium-ion batteries: a review. *Renew. Sust. Energy Rev.* **2025**, *207*, 114949.
15 Zhao, Y. Y.; Han, Y.; Yu, Y. J. Design of electronic conductive covalent-organic frameworks and their opportunities in lithium batteries. *Chem. Eng. J.* **2024**, *497*, 154997.
16 Liu, Z.; Zhang, X. C.; Luo, J. L.; Yu, Y. J. Application of metal-organic frameworks to the anode interface in metal batteries. *Chin. Chem. Lett.* **2024**, *35*, 109500.
17 Hlaing, M. T.; Gopalakrishnan, M.; Praserthdam, S.; Liu, W. R.; Mohamad, A. A.; Rajendran, S.; In, I.; Kheawhom, S. Carbon dots as multifunctional additives in zinc-ion batteries: progress, challenges, and opportunities. *Chem. Eng. J.* **2025**, *509*, 161327.
18 Dong, Y.; Hu, H. L.; Liang, P.; Xue, L. L.; Chai, X. L.; Liu, F. M.; Yu, M.; Cheng, F. Y. Dissolution, solvation and diffusion in low-temperature zinc electrolyte design. *Nat. Rev. Chem.* **2025**, *9*, 102–117.
19 Wang, Z. R.; Ni, Z. W.; Chen, J.; Dai, Y. M.; Gao, Y. S.; Zhang, Q.; Dong, F. B.; Xiong, S. L.; Zhang, C. H.; Feng, J. K. Recent progress and challenges on emerging high-entropy materials for better Zn-air and Zn-ion batteries. *Energy Storage Mater.* **2025**, *75*, 104064.
20 Zhao, Y. Y.; Feng, K. Y.; Yu, Y. J. In situ preparation of zincophilic covalent-organic frameworks with low surface work function and high rigidity to stabilize zinc metal anodes. *J. Energy Chem.* **2025**, *102*, 524–533.
21 Gupta, D.; Liu, S. L.; Zhang, R. Z.; Guo, Z. P. Future long cycling life cathodes for aqueous zinc-ion batteries in grid-scale energy storage. *Adv. Energy Mater.* **2025**, *15*, 2500171.
22 Ye, B. G.; Wu, F.; Zhao, R.; Zhu, H. H.; Lv, M. G.; Han, X. M.; Chen, T. D.; Wang, X. R.; Bai, Y.; Wu, C. Electrolyte regulation toward cathodes with enhanced-performance in aqueous zinc ion batteries. *Adv. Mater.* **2025**, *37*, 2501538.
23 Gou, Q. Z.; Zhang, S. D.; Mei, H. P.; Liu, C.; Luo, H. R.; Wang, K. X.; Hu, Y. Z.; Song, B. Y.; Zheng, Y. J.; Qiao, M. T.; Li, M. Construction of a robust cathode protection layer inspired by the wet adhesion behavior of mussels towards high-performance aqueous zinc-ion batteries. *J. Mater. Chem. A* **2025**, *13*, 7766–7776.
24 Mao, J. J.; Li, X. X.; Huang, Y.; Zhu, C. Y.; Yu, F. S.; Cheng, F. Nanorod-assembled urchin-like molybdenum–manganese oxide heterostructure with enhanced oxygen vacancies as a cathode for quasi solid state zinc-ion batteries. *J. Mater. Chem. A* **2025**, *13*, 9222–9232.
25 Ye, H. J.; Zeng, X. M.; Li, X. M.; He, K.; Li, Y. S.; Yuan, Y. F. Review of ion doping and intercalation strategies for advancing manganese-based oxide cathodes in aqueous zinc-ion batteries. *Nano Energy* **2025**, *136*, 110740.
26 Hu, X. Y.; Gao, S. Y.; Lin, T. G.; Peng, X. Y.; Huang, Y. X.; Zhang, Y. M.; Yang, X. C.; Wang, L. N.; Luo, G. F.; Wen, Z. H.; Johannessen, B.; Wang, S. C.; Wang, L. Z.; Luo, B. Iodine-doped sodium vanadate cathode for improved Zn ion diffusion kinetics. *Adv. Mater.* **2025**, *37*, 2416714.
27 Liu, H. B.; Hou, X. H.; Zhang, Q. C.; Peng, W. C.; Li, Y.; Fan, X. B. Representative by-products of aqueous zinc-vanadium batteries: origins, roles, strategies, and prospects. *Adv. Energy Mater.* **2025**, *15*, 2406171.
28 Pu, J. R.; Xue, Y. T.; Ji, Z. Y.; Cao, J. Y.; Shen, X. P.; Zhou, H. B.; Yuan, A. H.; Kong, L. R. Manganese octacyanomolybdate/carbon nanotube hybrids as novel cathode materials for aqueous zinc-ion batteries. *J. Colloid Interface Sci.* **2025**, *686*, 27–36.
29 Wang, D. H.; Qin, M. X.; Zhang, C. Y.; Li, M. X.; Peng, C.; Zhi, C. Y.; Li, Q.; Zhu, L. Enhancing organic cathodes of aqueous zinc-ion batteries *via* nitro group modification. *Chem. Sci.* **2025**, *16*, 3630–3637.
30 Zhu, Y. C.; Dong, Y. Z.; Li, J. G.; Li, Y. B.; Fan, Q. H.; Kuang, Q.; Zhao, Y. M. In situ electrochemical activation strategy toward organic

cation preintercalated layered vanadium-based oxide cathode for high-performance aqueous zinc-ion batteries. *ACS Appl. Mater. Interfaces* **2025**, *17*, 16791−16801.
31 Sajid, M.; Rahman, S. U.; Munsif, S.; Tao, F. Y.; Ali, U.; Ali, N.; Zhang, J. P. Carbonyl-enriched sulfide linked conjugated polymer as a cathode for aqueous zinc ion batteries. *J. Energy Storage* **2025**, *112*, 115512.
32 Guo, D.; Fan, Y.; Yang, Q.; Song, M. Z.; Zhang, F. Y.; Liu, J.; Zhu, Z. W.; Zhang, H. F. Oxygen-deficient organic/inorganic VO_x-PPy cathode composites: enabling prolonged lifespan of aqueous zinc-ion batteries. *Chem. Eng. J.* **2025**, *507*, 160745.
33 Gao, X. Y.; Wang, Y. W.; Xiao, Y. G.; Pan, R. N.; Liu, C. X.; Gong, Q.; Xu, K. G.; Xie, H. J.; Wang, G.; Ren, Y. C.; Gu, T. T. A new polymer with rich carbonyl delocalized π-conjugated structure for high-performance aqueous zinc ion batteries. *J. Colloid Interface Sci.* **2025**, *685*, 604−614.
34 Liu, S.; Sun, Z. W.; Li, B. G.; Liu, X. J.; Xue, C. G. Innovative cobalt manganese-based Prussian blue analogue/polyaniline cathode materials with double layered hollow nanocube structure for high performance aqueous zinc ion battery. *J. Energy Storage* **2025**, *111*, 115310.
35 Lai, X. J.; Li, Y. H.; Niu, J. F.; Li, J. T.; Cao, Y. H.; Liu, S. L.; Wang, C. Simultaneous electrodeposition of vanadium oxide and polyaniline derivatives and its application in aqueous zinc ion storage. *Chem. Eng. J.* **2025**, *509*, 161447.
36 Su, L. X.; Yang, B. Z.; Chen, X. J.; Lu, Y. W.; Zhang, H. M.; Jiang, Q. Y.; Liu, Q. An organic cathode integrating carbonyl and imino groups for high-performance aqueous zinc-ion battery with air self-charging ability. *J. Energy Storage* **2024**, *100*, 113680.
37 Zhou, W. B.; Yuan, S. B.; Ding, W. M.; Cao, Y.; Yang, Y.; He, Y.; Yang, Y. Q.; Li, X. M.; Luo, M. Organic-inorganic hybrids cathode with hydrogen bonding network for highly efficient zinc-ion batteries. *J. Energy Storage* **2025**, *104*, 114448.
38 Zhan, S.; Wang, C. F.; Zhong, L. H.; Zhao, L. W.; Yang, X. D.; Guo, A. X. Y.; Xiong, W.; Cheng, L. J.; Li, R.; Tang, Z. J.; Cao, S. C.; Zhi, C. Y.; Lv, H. M. Insight into anionic discrepancies in bipolar poly(thionine) organic cathodes for aqueous zinc ion batteries. *Small* **2024**, *20*, 2402767.
39 Du, D. W.; Zhou, J. Y.; Yin, Z. L.; Feng, G. Z.; Ji, W. X.; Huang, H.; Pang, S. P. High-voltage recyclable organic cathode enabled by heteroatomic substitution for aqueous zinc-ion batteries. *Adv. Energy Mater.* **2024**, *14*, 2400580.
40 Wang, C. D.; Li, Y. F.; Zhang, S. D.; Sang, T. Y.; Lei, Y.; Liu, R. Q.; Wan, F.; Chen, Y. J.; Chen, W. G.; Zheng, Y. J.; Sun, S. H. Organic cation-supported layered vanadate cathode for high-performance aqueous zinc-ion batteries. *Carbon Energy* **2025**, *7*, e647.
41 Zhang, C. H.; Li, F. K.; Gu, T. T.; Song, X.; Yuan, J. J.; Ouyang, L. Z.; Zhu, M.; Liu, J. Covalent organic frameworks for high-performance rechargeable lithium metal batteries: strategy, mechanism, and application. *Prog. Mater. Sci.* **2025**, *152*, 101455.
42 Lu, X. M.; Aslam, J.; Waseem, M. A.; Zhang, Y. F.; Sun, W. W.; Wang, Y. Harnessing interfacial engineering in covalent organic frameworks for lithium metal batteries. *Coord. Chem. Rev.* **2025**, *535*, 216604.
43 Yin, L. Y.; Guo, X. Y.; Hu, J. F.; Yan, K. M.; Liu, L.; Shi, X. Y.; Cui, F. C.; Zhu, G. S.; Zhang, N. Strategic nitrogen site alignment in covalent organic frameworks for enhanced performance in aqueous zinc-iodide batteries. *Angew. Chem. Int. Ed.* **2025**, *64*, e202423265.
44 Yi, P. S.; Li, Z. H.; Ma, L. L.; Feng, B. J.; Liu, Z.; Liu, Y. S.; Lu, W. Y.; Cao, S. C.; Fang, H. Y.; Ye, M. X.; Shen, J. F. Eco-friendly high-performance symmetric all-COF/graphene aqueous zinc-ion batteries. *Adv. Mater.* **2024**, *36*, 2414379.
45 Zhao, Y. Y.; Yang, C. T.; Yu, Y. J. A review on covalent organic frameworks for rechargeable zinc-ion batteries. *Chin. Chem. Lett.* **2024**, *35*, 108865.
46 Zheng, H.; Yan, W.; Zhang, J. J. Porous organic framework-based materials (MOFs, COFs and HOFs) for lithium-/sodium-/potassium-/zinc-/aluminum-/calcium-ion batteries: a review. *Electrochem. Energy Rev.* **2025**, *8*, 3.
47 Xu, J.; Yang, Y. T.; Dai, Q. Y.; Zheng, Z. Y.; Cao, Y. J.; Cheng, Y. W.; Peng, B.; Ma, L. B.; Wang, Y. G. Towards ultra-stable wide-temperature zinc-ion batteries by using ion-sieving organic framework membrane. *Angew. Chem. Int. Ed.* **2025**, *64*, e202423118.
48 Du, J. Y.; Zhan, X.; Xu, Y. H.; Zhang, D. H.; Qin, S. H. Heat-resistant covalent organic framework (COF) PVA-hybridized gel electrolyte for the preparation of dendrite-free zinc-ion batteries. *Nano Lett.* **2024**, *24*, 13592−13599.
49 Lu, H.; Meng, S.; He, T.; Zhang, C.; Yang, J. H. Recent progress in covalent organic frameworks for rechargeable zinc-based batteries. *Coord. Chem. Rev.* **2024**, *514*, 215910.
50 Kim, S.; Choi, H. C. Light-promoted synthesis of highly-conjugated crystalline covalent organic framework. *Commun. Chem.* **2019**, *2*, 60.
51 Meng, Z.; Aykanat, A.; Mirica, K. A. Proton conduction in 2D Aza-fused covalent organic frameworks. *Chem. Mater.* **2019**, *31*, 819−825.
52 Ma, D. X.; Zhao, H. M.; Cao, F.; Zhao, H. H.; Li, J. X.; Wang, L.; Liu, K. A carbonyl-rich covalent organic framework as a high-performance cathode material for aqueous rechargeable zinc-ion batteries. *Chem. Sci.* **2022**, *13*, 2385−2390.